

RESEARCH ARTICLE

10.1029/2018JA026093

Key Points:

- X-ray images are estimated based on MHD simulations under different solar wind conditions
- Responses of the magnetopause to solar wind changes are analyzed from X-ray images
- Responses of the cusp to solar wind variations are presented via X-ray images

Correspondence to:

C. Wang and T. R. Sun,
 cwang@spaceweather.ac.cn;
 trsun@spaceweather.ac.cn

Citation:

Sun, T. R., Wang, C., Sembay, S. F., Lopez, R. E., Escoubet, C. P., Branduardi-Raymont, G., et al. (2019). Soft X-ray imaging of the magnetosheath and cusps under different solar wind conditions: MHD simulations. *Journal of Geophysical Research: Space Physics*, 124, 2435–2450. <https://doi.org/10.1029/2018JA026093>









Received 23 SEP 2018

Accepted 7 FEB 2019

Accepted article online 13 FEB 2019

Published online 1 APR 2019

Soft X-ray Imaging of the Magnetosheath and Cusps Under Different Solar Wind Conditions: MHD Simulations

T. R. Sun¹ , C. Wang^{1,2} , S. F. Sembay³ , R. E. Lopez⁴ , C. P. Escoubet⁵ , G. Branduardi-Raymont⁶ , J. H. Zheng^{1,7}, X. Z. Yu¹, X. C. Guo¹, L. Dai¹ , Z. Q. Liu¹ , F. Wei¹, and Y. H. Guo¹

¹National Space Science Center, Chinese Academy of Sciences, Beijing, China, ²College of Earth and Planetary Sciences, University of Chinese Academy of Sciences, Beijing, China, ³Department of Physics and Astronomy, University of Leicester, Leicester, UK, ⁴Department of Physics, University of Texas at Arlington, Texas, USA, ⁵European Space Research and Technology Center, European Space Agency, Noordwijk, The Netherlands, ⁶Mullard Space Science Laboratory, University College, London, UK, ⁷School of Astronomy and Space Science, University Chinese Academy of Sciences, Beijing, China

Abstract The soft X-ray emissions from the Earth's magnetosheath and cusp regions are simulated under different solar wind conditions, based on the PPMLR-MHD code. The X-ray images observed by a hypothetical telescope are presented, and the basic responses of the magnetopause and cusp regions are discernable in these images. From certain viewing geometries, the magnetopause position in the equatorial plane, as well as the latitudinal scales and azimuthal extent of cusp can be directly extracted from the X-ray images. With these reconstructed positions, the issues we are able to analyze include but are not limited to the compression of magnetopause and widening of the cusp after an enhancement of solar wind flux, as well as the erosion of the magnetopause and equatorward motion of cusp after the southward turning of the interplanetary magnetic field. Hence, the X-ray imaging is an appropriate technique to study the large-scale motion of magnetopause and cusps in response to solar wind variations.

1. Introduction

The Earth's magnetopause is formed as a result of the interaction between the solar wind and the terrestrial magnetic field. Its existence was first predicted by Chapman and Bartels (1940). With the help of in situ satellites, we are able to assume that the magnetopause has been crossed if the instruments observe changes of plasma conditions (e.g., Ness et al., 1966). However, the large-scale magnetopause has never been “seen” as a whole. In situ measurements can provide detailed information about the local plasma and fields, whereas the sparse in situ detections exhibit limitations. For instance, it is difficult to reveal the temporal changes of the magnetopause during a single spacecraft crossing. Therefore, observations by in situ satellites are not sufficient to explain the coherent overall responses and evolutions of the magnetopause and cusps as well.

Recently, a novel approach was proposed to remotely detect the large-scale magnetopause: soft X-ray imaging (Branduardi-Raymont et al., 2012, 2016; Collier et al., 2012; Sibeck et al., 2018; Walsh et al., 2016). The basic mechanism for soft X-ray emissions in the magnetosheath and cusp regions is the solar wind charge exchange (SWCX) process. On the one hand, heavy ions in high charge states, such as O⁷⁺, exist in the ambient solar wind. On the other hand, neutral atoms and molecules, such as the hydrogen, are ubiquitous in the geospace environment due to the Earth's exosphere. When they encounter and interact with each other, an electron can be transferred from the neutral to the ion. As a result of capturing the electron, the solar wind ion is in an electronically excited state, and then emits one or more photons in the extreme ultraviolet or soft X-ray bands while decaying to the lower-energy state. In the magnetosheath, the density of the highly charged ions is enhanced as the solar wind slows down after the bow shock. The solar wind cannot directly penetrate the magnetopause, and thus, the plasma with solar wind origin is quite tenuous inside the magnetosphere. This leads to a sharp boundary at the magnetopause in terms of the soft X-ray emissivity. The cusps are special regions on the magnetopause. The solar wind plasma can enter directly, and thus, the X-ray emissivity is expected to be higher inside of the cusps. With different solar wind fluxes and/or interplanetary magnetic fields (IMF), the X-ray emissivity in the magnetosheath and cusps can be

apparently different. Therefore, information of magnetopause location and the cusp boundaries may be revealed by images detected with a soft X-ray telescope.

The SWCX emission of soft X-rays was first discovered from the ROSAT observation of comets (Cravens, 1997; Lisse et al., 1996), and then extended to the observation of planets and planetary satellites (e.g., Collier et al., 2014; Dennerl, 2002; refer to the review by Bhardwaj et al., 2007). In the geospace environment, the SWCX X-ray emission has also been detected but limited to a certain view direction within a quite narrow field of view (FOV). For instance, Snowden et al. (2009), Carter et al. (2010), and Fujimoto et al. (2007) reported SWCX emissions from the subsolar, flank magnetosheath, and the magnetic pole direction, respectively. It is difficult to extract information about the magnetopause position from the current data. In this context, the ESA-CAS joint mission, Solar wind-Magnetosphere-Ionosphere Link Explorer (SMILE), is proposed to achieve the objective of remotely detecting the large-scale magnetopause boundary (Branduardi-Raymont et al., 2016; Wang et al., 2017). It will have a Soft X-ray Imager (SXI) onboard, with a large FOV: $16^\circ \times 27^\circ$. The center of the SXI FOV will point to a location close to the subsolar magnetopause for most of the time on the orbit, which has an inclination angle of either $\sim 90^\circ$ or $\sim 67^\circ$. SMILE is planned to be launched around 2023.

As there is no X-ray image of the large-scale magnetopause observed so far, it is critical to simulate the soft X-ray emissions and analyze the information that can be extracted from the images. Cravens et al. (2001) developed a model for SWCX X-ray emissions (see section 2 for details). Based on this model, Robertson and Cravens (2003) and Robertson et al. (2006) first presented X-ray images of the magnetosheath (without and with cusps), by using numerical models to provide plasma parameters in the solar wind-magnetosphere system. X-ray images during a storm event were simulated by Branduardi-Raymont et al. (2016). Carter and Sembay (2008), Carter et al. (2010, 2011), and Whittaker et al. (2016) simulated the X-ray intensities from different view directions to compare with XMM-Newton observations, and the former three studies used an empirical model, whereas Whittaker et al. (2016) used an MHD model as the basis of the simulation. Wargelin et al. (2014) compared Chandra observations with simulation results based on very simple assumption of the plasma parameters in the magnetosheath. Connor and Carter (2017) selected a case of an XMM-Newton observation and compared the simulation result with observation in order to estimate the exospheric neutral density. Transient structures on the magnetopause such as flux transfer events and Kelvin-Helmholtz waves were also investigated numerically (Collier et al., 2010; Sun et al., 2015). Despite these studies, there are still some basic issues not sufficiently analyzed. One of the fundamental problems is whether the magnetopause responses to solar wind variations are discernable in the two-dimensional (2-D) X-ray images. The solar wind plasma conditions directly affect the three-dimensional (3-D) X-ray emissivity, but the magnetopause structures in an X-ray image may be blurred to some extent due to the line integration of the 3-D X-ray emissivity along a given line-of-sight. Will these effects be visible from the X-ray images? This paper will focus on problems such as how do the X-ray images vary under different solar wind conditions, and what can we estimate about the positions of magnetopause and cusps from the X-ray images, with a simulation model described in section 2. The results are analyzed in section 3, and summarized in section 4.

2. Model Description

2.1. X-ray Intensity

The model we use to calculate the X-ray intensity along a given direction (I_X) is similar to that described by Sun et al. (2015), which is the line integration of the X-ray emissivity P_X :

$$I_X = \frac{1}{4\pi} \int P_X dr = \frac{1}{4\pi} \int \alpha_X n_H n_{sw} \langle g \rangle dr \quad (\text{keV} \cdot \text{cm}^{-2} \cdot \text{s}^{-1} \cdot \text{sr}^{-1}), \quad (1)$$

α_X , n_H , n_{sw} , and $\langle g \rangle$ in this equation are the interaction efficiency factor, number density of exospheric hydrogen, solar wind plasma density, and the relative velocity, respectively. The α_X value is dependent on the charge transfer cross section, the fraction of high charge state ion species in the solar wind, transition energy, etc. According to the studies by Cravens (2000), Pepino et al. (2004), Wargelin et al. (2014), Kuntz et al. (2015), and Whittaker and Sembay (2016), 1×10^{-15} eV cm^2 used in the current simulation is a reasonable or conservative estimation for α_X under the average solar wind speed (~ 400 km/s). The number density of exospheric hydrogen is approximated by $n_H = n_0 (10R_E/r)^3 \text{ cm}^{-3}$, where $n_0 = 25$ is adopted in this paper following Cravens et al. (2001). Connor and Carter (2017) simulated an event and gave a higher n_0 with 47 cm^{-3} , which implies that our study here may provide a conservative estimate of the X-ray signals.

Table 1
The Solar Wind Parameters Setup for Simulation Runs

Run	Number density (cm ⁻³)	Velocity V_x (km/s)	B_z (nT)
Case 1	5	400	-5
Case 2	20	400	-5
Case 3	35	400	-5
Case 4	12.5	400	5
Case 5	12.5	400	-5

Other empirical neutral density models (e.g., Hodges, 1994) predict quite similar values at the subsolar magnetopause, but the discrepancy becomes somewhat larger in the cusp regions at a lower geocentric distance. Nevertheless, the selection of n_0 or the neutral density models has no apparent influence on the analysis of boundary positions, other than it affects the overall X-ray intensity on the image and hence the detectability of such features in the presence of background noise. The relative velocity is $\langle g \rangle = \sqrt{u_{sw}^2 + u_{th}^2}$, where u_{sw} and u_{th} are the plasma bulk velocity and the thermal speed, respectively. The integration of P_X goes from the observation point to $r = 80R_E$, beyond which the X-ray emissivity is negligible due to very sparse geocoronal hydrogen. Although for the SMILE orbit with apogee at $20 R_E$, an integration distance with $50\text{--}60 R_E$ is sufficient, $80 R_E$ used in this paper can make sure that the neglected emissions further away will not cause any problem.

2.2. Model for the X-Ray Emissions

A global MHD code simulating the solar wind-magnetosphere-ionosphere coupling system, namely PPMLR-MHD code (Piecewise Parabolic Method with a LagRangian remap, refer to Hu et al. (2007) for details of the code), was run to provide the parameters required in Equation (1): n_{sw} , u_{sw} , and u_{th} . These parameters are physical quantities for the solar wind plasma. Nevertheless, the MHD code itself does not differentiate solar wind plasma and magnetospheric plasma. Therefore, number density and velocity obtained from the MHD simulations cannot be directly used to calculate the X-ray emissivity. To solve this problem, we first find out the boundary position where the solar wind plasma cannot directly come across (i.e. the inner magnetosphere) from the MHD simulations, and then set the parameters inside this boundary to be zero. Although there is indirect access of solar wind particles into the magnetosphere, the X-ray intensity inside the magnetosphere is at least an order of magnitude smaller than the outside (Sun et al., 2015). Therefore we neglect this part in the present study. A possible limitation of this process is: if the identified magnetopause position is close to the center or the outer edge of the boundary layer, some inner part of the boundary layer is not able to be included in the results. Therefore, several methods for the boundary identification have been tested, and the one that returns a location close to the inner edge has been selected (further explained in section 2.2.2).

2.2.1. The Setup for Simulation Runs

Five simulation runs are studied in this paper, with the main solar wind parameters listed in Table 1 for each run. Other input parameters are the same: velocity $V_y = V_z = 0$, IMF $B_x = B_y = 0$, and thermal pressure $p = 0.0125$ nPa. Cases 1–3 are compared to show the influence of solar wind flux (density), which is 2.0×10^8 , 8.0×10^8 , and 1.4×10^9 cm⁻² s⁻¹, respectively. We expect that the effects of flux increase caused by the enhancement of solar wind velocity are similar, only that α_X in equation (1) tends to be smaller for higher-speed case (Pepino et al., 2004). Cases 4 and 5 are analyzed to show the difference caused by IMF B_z . High spatial resolution ($\sim 0.1 R_E$ near the subsolar magnetopause) was employed in the simulations. A uniform resistivity ($\eta = 7.5e4H$ m/s) is used in the code to reduce the production rate of flux transfer events (FTEs), so that we can get a smooth magnetopause and focus on the large scale configuration of magnetopause on the X-ray image. A more detailed discussion will be given in future studies about the small-scale structures such as FTEs. The inner boundary of the magnetospheric domain is a spherical shell with $r = 3R_E$, which is coupled to the ionosphere through Earth's dipole field. This study assumes a uniform Pedersen conductance ($5 S$) and a zero Hall conductance in the ionosphere. Dipole tilt is set to zero and the geocentric solar magnetospheric (GSM) coordinates are used. The MHD model has been run with constant parameters until it settles into an equilibrium state.

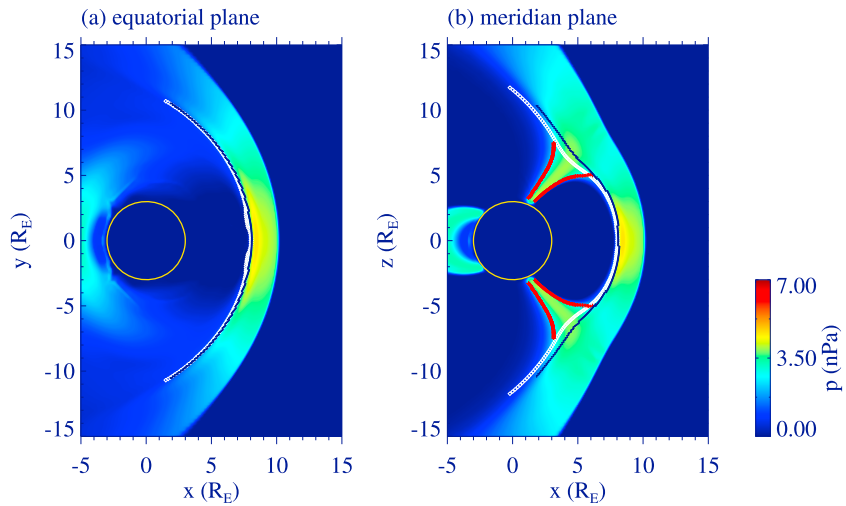


Figure 1. Positions of magnetopause (white lines) and cusps (red lines) in the equatorial (a) and noon-midnight meridian (b) plane. The backgrounds are contours of the thermal pressure. The yellow circles show the inner boundary of the magnetohydrodynamic simulation domain.

2.2.2. Magnetopause Position

The position of magnetopause was determined by using a “tracer method” (Florinski et al., 2013). We introduce the variable Q as an indicator for the origin of each fluid element. It is set to 1 at the inflow boundary of the code at $x = 30R_E$, and it flows together with each fluid element. $Q = 1$ at a certain location indicates that if the fluid element at this location is traced backward in time, it can be traced into the solar wind (i.e., this fluid element comes from the solar wind). If $Q = 0$ at a certain location, the fluid element cannot be traced back to the solar wind, and therefore, this is the region where the solar wind plasma cannot directly penetrate (i.e., the magnetosphere). Therefore, the condition $0 < Q < 1$ basically indicates the location of the magnetopause. In the code, Q is applied with the existing MHD variables by numerically solving the continuity equation (ρ and \mathbf{V} are plasma density and velocity, respectively).

$$\frac{\partial(Q\rho)}{\partial t} + \nabla \cdot (Q\rho\mathbf{V}) = 0, \quad (2)$$

The white lines in Figure 1 ($Q = 0.8$) shows the magnetopause determined by using this method for Case 2. The background colors represent contours of thermal pressure in the equatorial and noon-midnight meridian plane, respectively. We have also tested other methods for boundary identification, for instance, maximum current density location, maximum density gradient (see the black lines in Figure 1), the innermost stream line, etc. The results given by all these approaches are basically consistent with each other, but the tracer method provides a more smooth boundary compared to others. It can also give a magnetopause position close to the inner boundary of the magnetopause boundary layer, so that the effect of boundary layer can be included in the study. Thus, it is used in the present paper.

2.2.3. Cusp Positions

As all the boundary identification methods mentioned above fail to provide a magnetopause with cusps extending deeply to the lower altitude, a new method is developed to determine the cusp boundaries. We study the contours of thermal pressure on a series of spherical shells starting from a radius slightly larger than the inner boundary of the MHD code (starting from $r = 3.5R_E$ here). On each spherical shell, the location with the maximum thermal pressure p_{\max} is the center of the cusp region, and the boundary of cusps is defined by the location where thermal pressure decreases to 60% of p_{\max} . Considering that the thermal pressure decreases sharply near the cusp boundaries, other criteria such as 70% $\times p_{\max}$ or 50% $\times p_{\max}$ do not make a significant difference. Figure 2 shows the contours of thermal pressure on four typical spherical shells from lower to higher altitudes for Case 2. The black lines depict the contour of 60% $\times p_{\max}$ for each altitude, respectively. When the black line apparently deforms toward the low latitude (lower right panel in Figure 2), we stop the cusp identification program. The 3-D view of the northern cusp is given in Figure 3a, which shows a funnel-shaped structure. The azimuthal scale of the cusp is larger than the scale along north-south

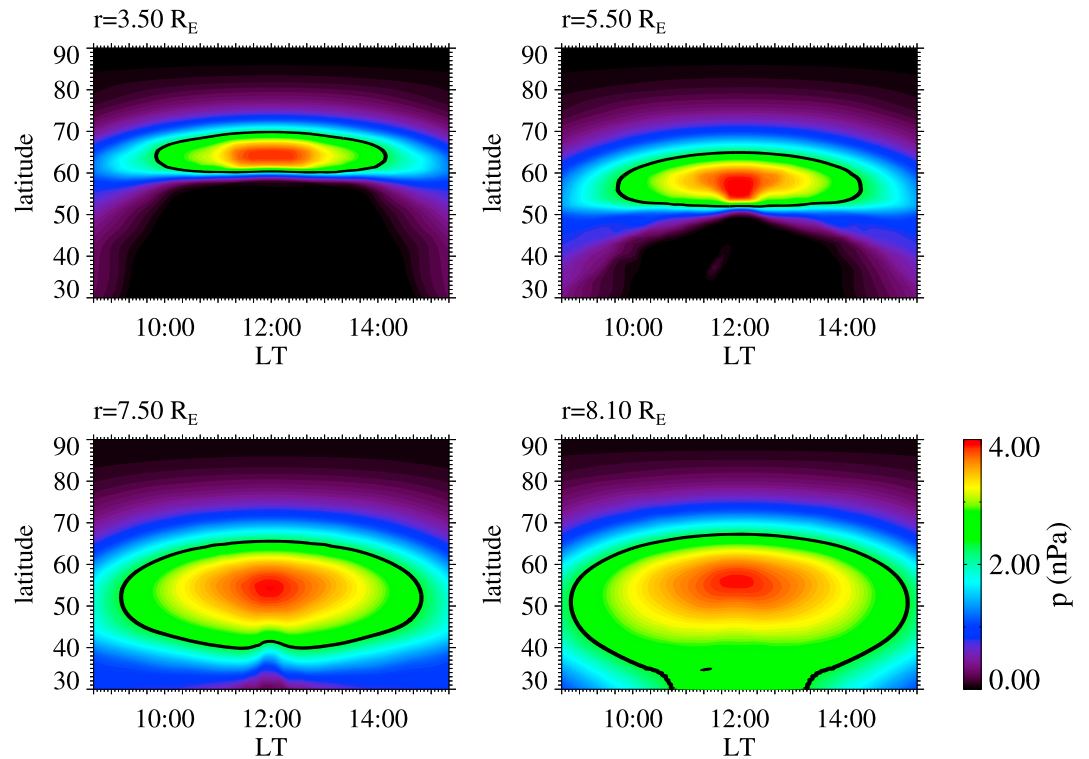


Figure 2. Contours of thermal pressure on four spherical shells with $r = 3.5R_E, 5.5 R_E, 7.5 R_E,$ and $8.1 R_E$. The black lines mark the cusp boundaries.

direction, corresponding to a shape similar to an ellipse on each altitude (see Figure 2). Figure 3b illustrates the 3-D magnetopause with cusps.

The cusp boundaries in this MHD simulation are comparable to statistical studies based on satellite data. Newell and Meng (1994) analyzed the Defense Meteorological Satellite Program (DMSP) data and concluded that the local time extent of the cusp region enhances if the solar wind dynamic pressure P_d increases. In their study, the cusp region mainly locates within 11:00–13:00 LT for the data group with $P_d < 2$ nPa and extends to 10:00–14:00 for cases with $P_d > 4$ nPa. The simulation runs studied here provide a similar trend:

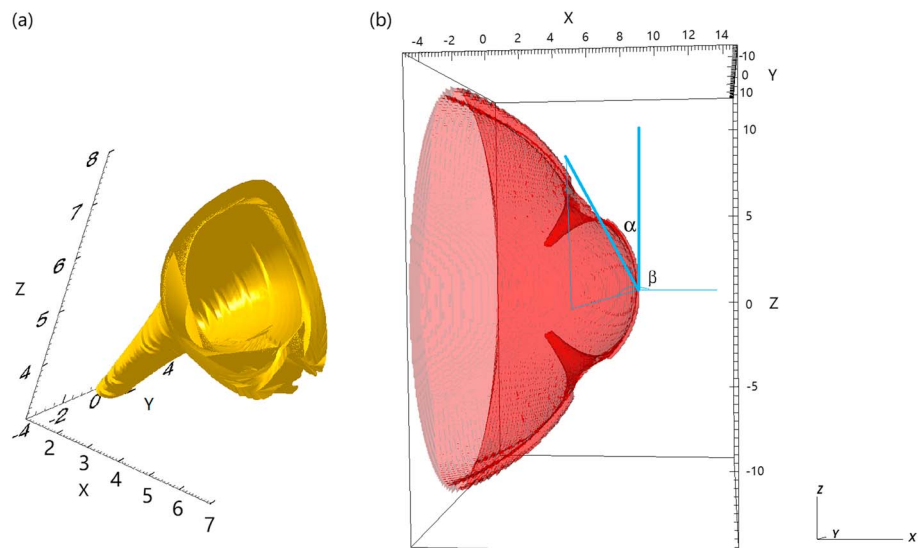


Figure 3. Three-dimensional views of northern cusp (a) and the magnetopause with cusps (b).

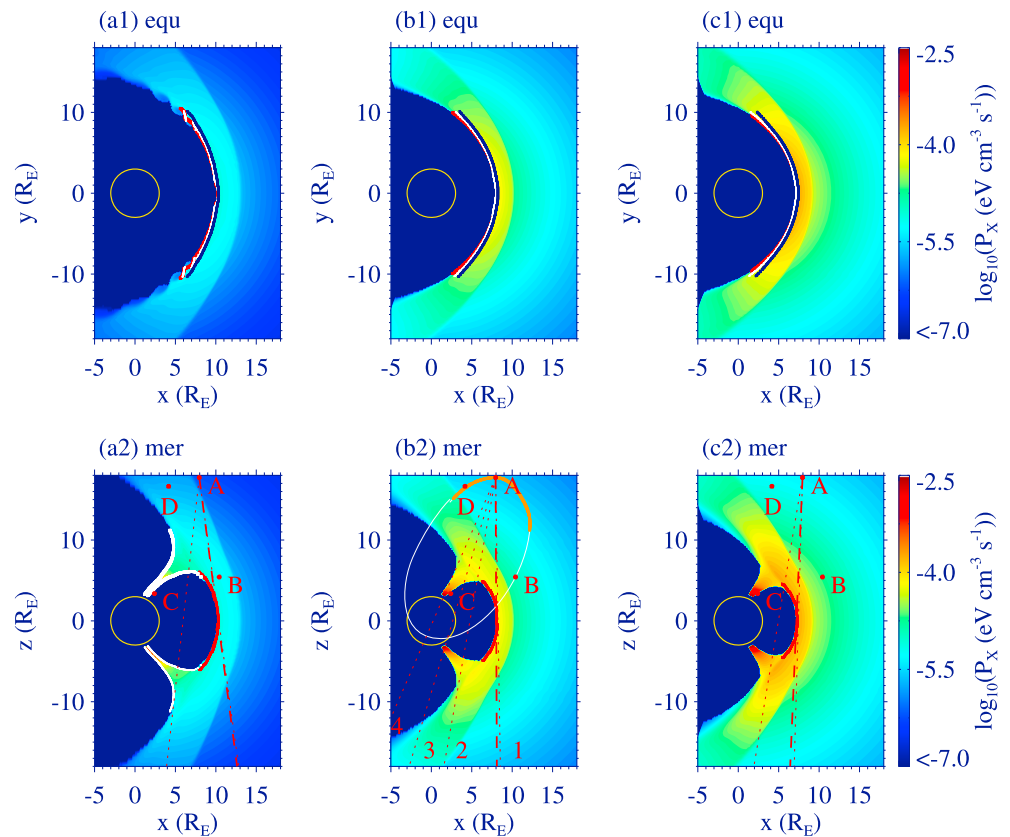


Figure 4. The X-ray emissivity P_X in the equatorial plane (a1, b1, c1) and the noon-midnight meridian plane (a2, b2, c2) for Cases 1–3. Contours of $\log_{10}P$ are plotted under different solar wind fluxes: Cases 1 (a1 and a2), 2 (b1 and b2), and 3 (c1 and c2). The red curves are magnetopause position in magnetohydrodynamic simulation. The white and black curves in (a1, b1, c1) are magnetopause identified from the X-ray images by using maximum dI_x and I_x , respectively. The white lines in (a2) show the boundaries for northern (thick) and southern (thin) cusps. In (b2), the white curve is a typical orbit for SMILE with $\sim 90^\circ$ inclination in the geocentric solar magnetospheric coordinate. Points A–D are projections onto the X - Z plane of four satellite positions discussed in the text. Red thin dotted lines marked by numbers 1 to 4 are line of sights corresponding to the peaks of X-ray intensity in Figure 5, and the red thick dashed lines are directions for the maximum gradient of X-ray intensity in Figure 5. SMILE = Solar wind-Magnetosphere-Ionosphere Link Explorer.

10:40–13:20 LT for Case 1; 09:52–14:08 LT for Case 2; and 09:44–14:16 LT for Case 3. The local time extent under the southward and northward IMF does not show much difference in our simulations. The latitude of the cusp region is basically related to the IMF B_z direction. It is observed to move equatorward when the IMF turns from northward to southward according to Newell et al. (1989), Escoubet et al. (2006), and Pitout et al. (2006). In the PPMLR-MHD simulations, the trend of latitudinal variation is consistent with observational studies. The latitudinal extent of the cusp in this MHD simulation tends to be wider than observation. Pitout et al. (2006) gave an empirical equation for the cusp edges under different IMF B_z conditions, and the cusp latitude is $74.3\text{--}75.8^\circ$ for IMF $B_z = -5$ nT according to their statistics (1.5° wide). With the solar wind plasma conditions not mentioned in that paper, direct comparison with the MHD result is prevented. But still, we can see that the latitudinal width is relatively large in MHD (3.6° for Case 1). One possible reason is that the high numerical resistivity used in this study makes the cusp boundaries wider and thus expands the latitudinal extent. Another reason could be that the $0.1 R_E$ spatial resolution is not high enough for the study of cusp boundaries. Moreover, some processes occurring in cusps such as the particle precipitation are not able to be well reproduced by MHD simulation. Therefore, we would not expect the MHD results to exactly match with observation. This can be improved by reducing resistivity in the code, and also by increasing grid resolution (Zhang et al., 2013). But it is noted that a relatively wider cusp along the latitudinal direction does not have a marked effect while exploring problems such as whether the boundary positions can be derived from X-ray images.

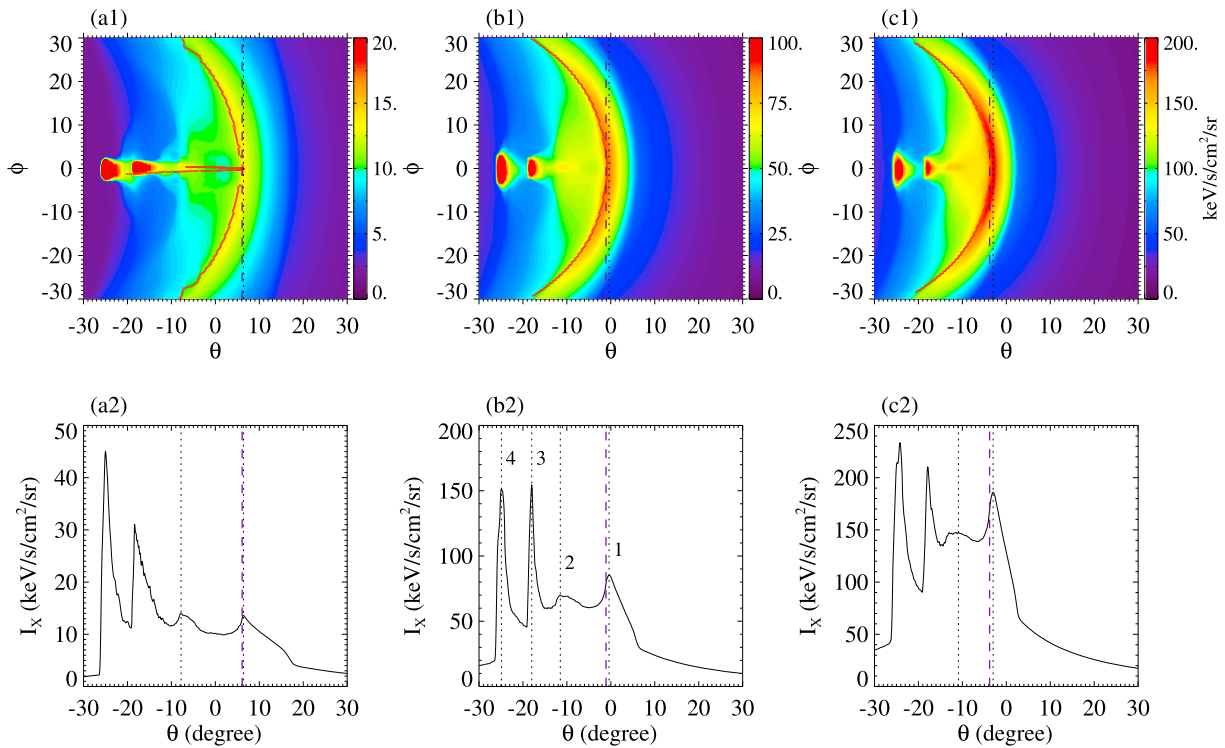


Figure 5. X-ray images of the magnetosheath and cusps for Cases 1 (a1), 2 (b1), and 3 (c1) with a special viewing geometry. The hypothetical satellite is at $(7.95, 0.32, 17.73) R_E$ indicated by point A in Figure 4, with the X-ray telescope pointing to $(8.37, 0, 0) R_E$. Red lines show the mapping of the equatorial magnetopause in Figures 4a1, 4b1, and 4c1 to the image coordinate. The magnetopause in the noon-midnight meridian plane in Figure 4 (a2) is also mapped to the image coordinate for Case 1 (red lines in Figure 5a1). The dashed and dotted lines mark the subsolar magnetopause identified by $\max(I_X)$ and $\max(dI_X)$, respectively. The lower panels show the dependence of X-ray intensity on the θ angle at $\phi = 0^\circ$, corresponding to each simulation case. The four peaks of I_X are labeled by the numbers 1–4.

3. Simulation Results

3.1. X-Ray Emissivity

The X-ray emissivity P_X under different solar wind conditions (Cases 1–3) is shown in the equatorial and the noon-midnight meridian planes in Figure 4. The upper panel shows that the maximum P_X is near the subsolar magnetopause for both low and high solar wind fluxes. In the meridian plane, maximum P_X occurs in the cusp region where the neutral density is higher. P_X near the subsolar magnetopause is enhanced with an increasing solar wind number density, and the reasons for this enhancement are as follows: (1) increased number density in the solar wind, (2) increased thermal pressure in the magnetosheath caused by a stronger bow shock, and (3) larger neutral density as the magnetopause is closer to the Earth. The former two facts also result in the enhancement of P_X in the cusp. Wave-like structures are seen at the flank magnetopause in Figure 4a1, which are related to the development of Kelvin-Helmholtz instability (KHI). KHI tends to be suppressed by the rise in n_{sw} in Figures 4b1 and 4c1.

3.2. Responses of Magnetopause to Solar Wind Changes Analyzed from the X-Ray Images

Although the effects of solar wind changes can be revealed by the X-ray emissivity as discussed in section 3.1, it is not straightforward to answer the question whether these responses are discernable in the 2-D images observed with an X-ray telescope. Due to the line integration of P_X along a given line of sight, there is a possibility that the magnetopause structures might be somewhat obscured by emissions elsewhere along the line. So this section will analyze the features of magnetopause from the perspective of X-ray images and try to find out what kind of information the X-ray images can provide us.

Assume that there is an idealized telescope at a potential position of SMILE: $(7.95, 0.32, 17.73) R_E$ pointing toward $(8.37, 0, 0) R_E$. This is an appropriate viewing geometry near the apogee of an orbit with $\sim 90^\circ$ inclination, which allows SXI to have a good coverage of the magnetopause close to the subsolar region. The white ellipse in Figure 4b2 is the projection of that orbit to the GSM XZ plane, and point A is the satellite position. The X-ray images expected to be seen by the telescope are depicted in the upper panel of Figure 5. The images

Table 2
Position of Magnetosphere Subsolar Point for Different Solar Wind Conditions

Run	Case 1	Case 2	Case 3	Case 4	Case 5
Subsolar from MHD - $\max(dN)$ (R_E)	10.3	8.1	7.3	9.0	8.7
Subsolar from X-ray - $\max(dI_x)$ (R_E)	10.3	8.0	7.2	8.9	8.6
Subsolar from X-ray - $\max(I_x)$ (R_E)	10.4	8.2	7.4	9.2	8.8

Note. MHD = magnetohydrodynamic.

are in $\theta - \varphi$ coordinate, with (0, 0) corresponding to the direction of the telescope pointing and the positive θ directed toward the Sun. The line integrated X-ray emission (I_x) are shown for Cases 1–3 with different solar wind flux. To the left of each image, the two red regions with very high X-ray emissions are the cusps. It is visible on the figure that the two bright regions are compressed along the θ direction and expand on the φ direction from Cases 1 to 3, showing the variations in the shape of cusps. The southern cusp is observed closer to the Earth due to a projection effect from the view point. It is also seen that there is a red-to-orange region on the right side of each image, mainly due to the enhancement of the X-ray emissivity in the magnetosheath. This region is compressed and moves toward the negative θ direction with increased solar wind flux. The X-ray intensities are apparently enhanced both in the magnetosheath and the cusp regions.

We would expect that the earthward edge of this crescent-shaped region implies the position of magnetopause (red arcs in Figure 5 are plotted by directly mapping the magnetopause identified from MHD results to the image coordinate). Actually, if there were no boundaries at all, the X-ray intensity would be expected to change smoothly. And thus the location with a sharp variation of I_x could potentially indicate the position of a boundary. The variations of I_x with θ along the $\varphi = 0^\circ$ direction are plotted in the lower panel of Figure 5. The maximum gradient ($\max(dI_x)$) near the magnetopause is marked by the thick dashed line in each plot of Figure 5. The direction corresponding to this maximum gradient is shown by the thick dashed lines labeled “1” in Figure 4. It is visible that this direction roughly traverses the subsolar magnetopause for the specific viewing geometry, as the satellite is almost right above the subsolar point. So we use this direction to estimate the location of the subsolar point. The magnetopause positions derived from this $\max(dI_x)$ method are listed in the second row of Table 2 for each studied case. Compared to the first row, showing the subsolar magnetopause directly identified from MHD results by using the maximum gradient of number density $\max(dN)$, it is seen that the analysis based on X-ray images provides a fairly good estimation of the subsolar point.

An alternative approach has been proposed by Collier and Connor (2018) to derive the magnetopause position. They gave a more general conclusion: the direction of the peak emission, that is, $\max(I_x)$ marked by the rightmost thin dotted lines in Figure 5, coincides with the tangent direction of the magnetopause. Applied to the specific viewing geometry here, the tangent direction roughly indicates the subsolar point of the magnetopause. Consequently, the information about subsolar point can be obtained by analyzing the peak direction, shown by the rightmost thin dotted lines in Figure 4. The third row in Table 2 lists the subsolar positions identified by this $\max(I_x)$ method. The difference between this and the MHD result is basically on the scale of $\sim 0.1 R_E$, which is the minimum grid size of the simulation code. Table 2 shows that the analysis of subsolar magnetopause from the X-ray image (both by $\max(dI_x)$ and $\max(I_x)$) provides reasonable results. Nevertheless, it is also noticed that the subsolar points in the third row are systematically larger than that in the first row, indicating that the magnetopause determined by using the maximum I_x direction tends to be closer to the outer boundary of the magnetopause boundary layer, which is more evident under northward IMF (Case 4). The values determined by the $\max(dI_x)$ method are roughly equal to but sometimes slightly smaller than the MHD results, implying that the $\max(dI_x)$ direction is in the vicinity of the center or inner boundary of the boundary layer. This effect is more evident toward the flanks of the magnetopause, which will be shown later. Here we emphasize that both methods can be used to analyze the magnetopause positions from X-rays, although they return slightly different positions in the boundary layer. Given that the grid resolution of the MHD model is around $0.1 R_E$ near the subsolar point, these results are mainly within the accuracy of the model. In the rest of the paper, we mainly use the $\max(dI_x)$ method.

Peaks “3” and “4” in Figure 5b2 are caused by the inner boundary of the MHD code at $r = 3R_E$. The red thin dotted lines marked by “3” and “4” in Figure 4b2 are the directions corresponding to the two peaks,

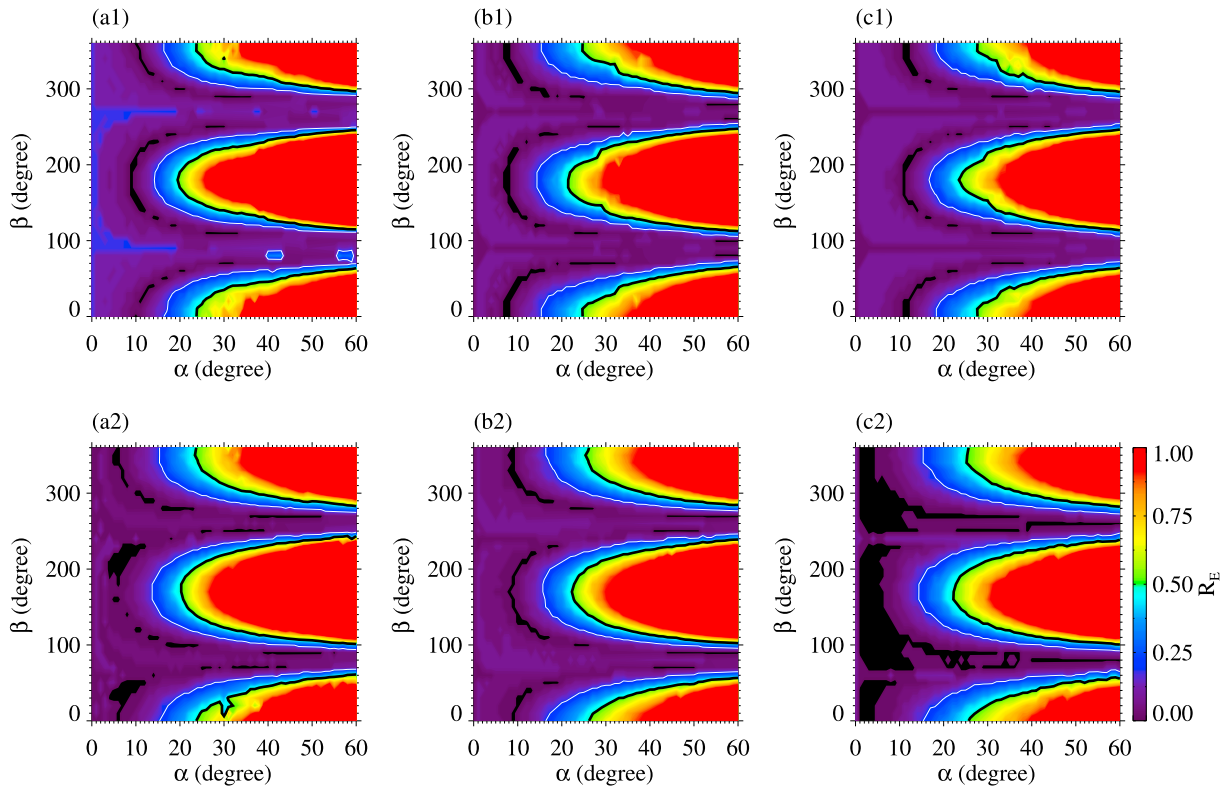


Figure 6. The dependence of magnetopause deviation dr on the α and β angles at the subsolar magnetopause (a1, b1, and c1) and at 14:00 LT on the equatorial magnetopause (a2, b2, and c2). The plots are for Cases 1, 2, and 3 from left to right. The white and black curves show the contours with $dr = 0.2R_E$ and $dr = 0.5R_E$, respectively.

traversing the low-altitude boundary of the cusp regions in the code. The X-ray emissivity is set to zero lower than this altitude because the MHD code is not able to simulate that region. This leads to the sudden decrease of I_x toward the negative θ direction, causing peaks 3 and 4. While in reality, it is expected that the strong X-ray emission from cusps would further extend toward the Earth inside this boundary, due to an even higher neutral density. Although the direction “2” in Figure 4b2 goes through the magnetosphere with zero emissivity, X-ray emissions from the magnetosheath, southern cusp, and even a little bit northern cusp all contribute to the line-integrated X-ray intensity, forming the peak 2 in Figure 5b2.

To quantify the error introduced by analyzing the X-ray images, we define $dr = |r_{\max(dN)} - r_{\max(dI_x)}|$, where $r_{\max(dN)}$ is the magnetopause position identified in the MHD result by finding the maximum gradient of density, and $r_{\max(dI_x)}$ is derived from the X-ray image by using the $\max(dI_x)$ method. The value of dr is related to the viewing geometry. At the subsolar point, the correlation between dr and the α and β angles is illustrated in the upper panel of Figure 6 for Cases 1–3. Here, α is defined as the angle between the line of sight and the z axis, illustrated in Figure 3b. β is the angle between the normal of the magnetopause (along the X axis at the subsolar point) and the projection of the line of sight to the equatorial plane. Figure 6 suggests that (1) the optimal viewing geometry is perpendicular to the normal of the magnetopause; that is, $\beta \sim 90^\circ$, $\beta \sim 270^\circ$, or $\alpha \sim 0^\circ$, and (2) for any given β , the subsolar magnetopause under low/high solar wind flux can be well identified by the $\max(dI_x)$ method if $\alpha < 14^\circ$, with an error smaller than $0.2R_E$. If the requirement of error is relaxed to $0.5R_E$, the method is feasible with $\alpha < \sim 20^\circ$. A large proportion of the SMILE orbit would ensure a viewing geometry with the required α angle (see the orange part of the orbit in Figure 4b2).

Not only limited to the subsolar point, the X-ray image can also be used to analyze the magnetopause position further toward the flanks of the magnetopause with certain constraints. The lower panel of Figure 6 shows the relationship between dr and the viewing geometry at 14:00 LT, 30° duskward of the subsolar point. A pattern quite similar to the upper panel is shown, and the criterion to use the $\max(dI_x)$ method is also $\alpha < \sim 20^\circ$. For the satellite position analyzed here, at $(7.95, 0.32, 17.73)R_E$, alpha is smaller than 20° at this local time, and thus the magnetopause position can be derived from the X-ray image via the $\max(dI_x)$

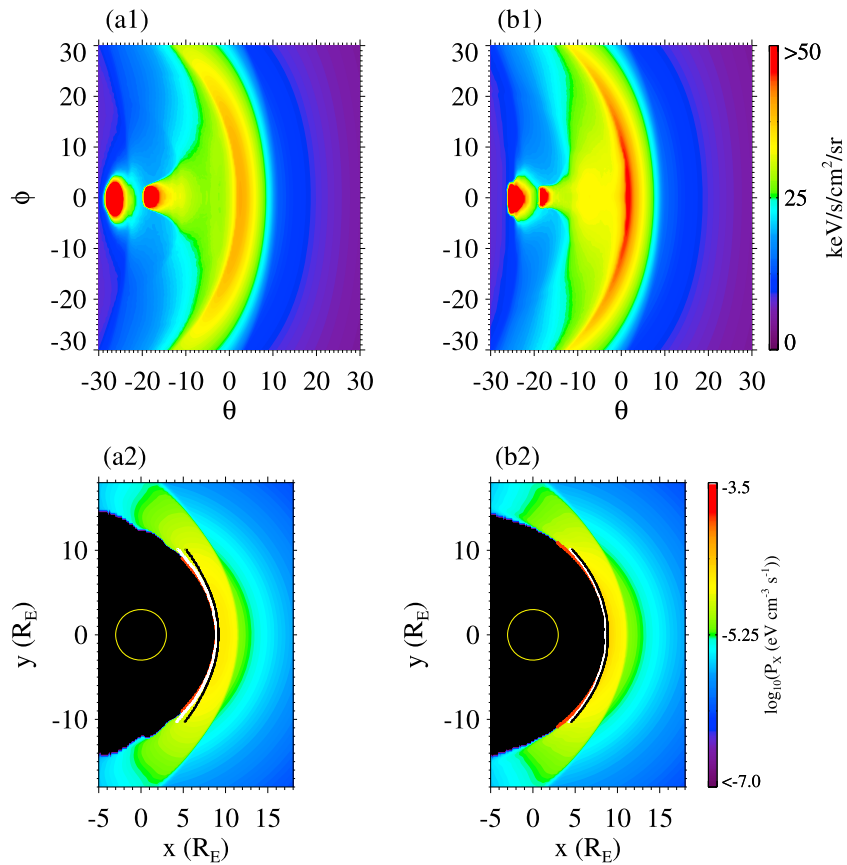


Figure 7. The X-ray images for Cases 4 (a1) and 5 (b1), with the same viewing geometry as Figure 5. The contours of X-ray emissivity in the equatorial plane are shown on the lower panels, (a2) and (b2), for both simulation runs. The red curves in (a2) and (b2) are the magnetopause identified from the magnetohydrodynamic simulation results. And the white and black curves are magnetopause reconstructed from the X-ray images by using $\max(dI_x)$ and $\max(I_x)$, respectively.

method. Actually, for the studied cases, the criteria is satisfied for the magnetopause roughly between 09:00 and 15:00 LT. We reconstruct this part of the magnetopause position in the equatorial plane, portrayed by the white curves in the upper panel of Figure 4. Compared to the red curves identified directly from the MHD results, it is visible that the magnetopause position derived from the X-ray image is in good accordance with the MHD result. The KH waves in Figure 4a1 can be revealed by this reconstruction. Also plotted in Figure 4 is the magnetopause analyzed via the $\max(I_x)$ method, shown by the black curves. It is seen that this method returns a magnetopause slightly sunward of the one shown by the red/white curve, which is even more notable toward the flanks and for the northward IMF case in Figure 7a2. In Figure 4a1, the signature of the KH wave is not evident in the black curve, as the $\max(I_x)$ method tends to give the outer boundary of the magnetopause boundary layer where the plasmas from the magnetosphere and magnetosheath are not fully mixed. We suggest that the distance between magnetopause positions identified by the $\max(dI_x)$ and $\max(I_x)$ methods can be used to study the thickness of the boundary layer.

Figure 7 shows the X-ray images and the magnetopause positions for Cases 4 and 5, which are the quasi-steady results under constant northward and southward IMF, respectively. The viewing geometry is the same as that in Figure 5. The X-ray emissivity shown in the lower panel indicates that P_x increases for southward IMF. The erosion of magnetopause as a final result of the magnetic reconnection is an important reason for this enhancement, as the neutral density becomes larger closer to the Earth. At a higher latitude, the plasma velocity as well as thermal pressure in the vicinity of the magnetopause are also increased by the reconnection process. From the X-ray images in the upper panel, it is visible that the earthward edge of crescent-shaped region slightly shifts toward the negative θ direction for the southward IMF case, indicative of an erosion of the magnetopause. The magnetosheath becomes slightly brighter under southward IMF,

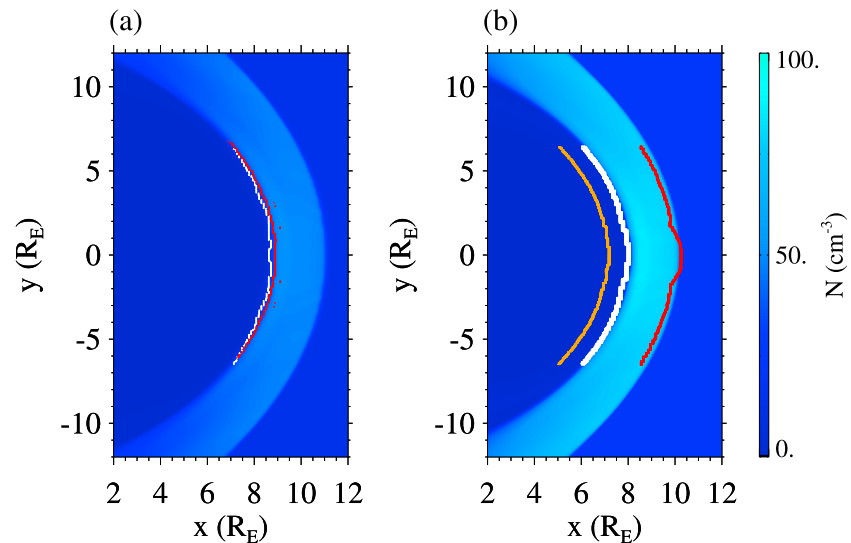


Figure 8. The magnetopause reconstructed from the X-ray image under different solar wind conditions. The $\max(dI_x)$ method is used here. Panel (a) shows the magnetopause positions for Cases 4 (red curve) and 5 (white curve). The background is the contours of plasma number density in the equatorial plane for Case 4. Panel (b) compares the magnetopause position under different solar wind fluxes, with the red, white, and yellow curves illustrating the magnetopause for Cases 1–3, respectively. The background shows the contours of number density for Case 2.

particularly evident in the region closer to the magnetopause. Derived from this image, the magnetopause in the equatorial plane is illustrated by the white (using the $\max(dI_x)$ method) and black ($\max(I_x)$ method) curves in Figures 7a2 and 7b2. The red curve portrays the MHD magnetopause. A good consistency between the MHD results and the X-ray analysis confirms that the magnetopause configurations and variations are discernable in images detected by a hypothetical soft X-ray telescope.

With these reconstructed magnetopause positions, the response of the magnetopause to solar wind changes can be quantitatively analyzed by direct comparison. Table 2 compares the subsolar points, and Figure 8 plots the magnetopause positions in the equatorial plane for all the studied simulation runs, extracted from the X-ray images. The background shows the contours of plasma number density in the equatorial plane for Cases 4 (left) and 2 (right). Both Table 2 and Figure 8a show that the magnetopause has an inward motion, from the red to the white curve, if the IMF orientation changes from northward to southward. The erosion is due to the occurrence of dayside reconnection. This earthward motion is more notable in the vicinity of the subsolar point than the flanks, which causes the shape of the magnetopause to become blunter. It is indicative of a higher reconnection rate around local noon. In Figure 8b, the red, white, and orange curves compare the magnetopause under different solar wind fluxes. Higher solar wind flux directly leads to the compression of the magnetopause, causing self-similar changes in the shape of the magnetopause. Therefore, from the different ways of variations on the X-ray images (e.g., self-similar or location-dependent boundary variations), we are able to analyze and reveal the magnetopause responses to different solar wind parameters (e.g., flux enhancement or IMF direction turning), which alter the magnetopause position and shape in different ways.

3.3. Response of Cusp to Solar Wind Changes Analyzed from the X-ray Images

If the hypothetical satellite moves to point B on the orbit shown in Figure 4b2, that is, it is at $(10.42, -0.0062, 5.43) R_E$ pointing to $(6.33, 0, 0) R_E$, the southern cusp shifts toward the center of the X-ray image. The upper panel in Figure 9 presents the X-ray images for Cases 1–3 with different solar wind fluxes under the quasi-steady condition, and the bright region to the left of the magnetosheath in each image is the southern cusp. It is clear that with increasing solar wind flux, the X-ray intensity from the cusp region is strikingly enhanced (note the color scale is different in the three panels). The scale of cusp along the θ direction is reduced, due to the compression of the solar wind. The enhancement of the cusp dimension along the φ direction is also discernable in the figure.

To discern the cusp boundary (along φ direction) from an X-ray image is relatively straightforward, as the X-ray intensity in the cusp region exhibits a very sharp increase superimposed on a relatively uniform

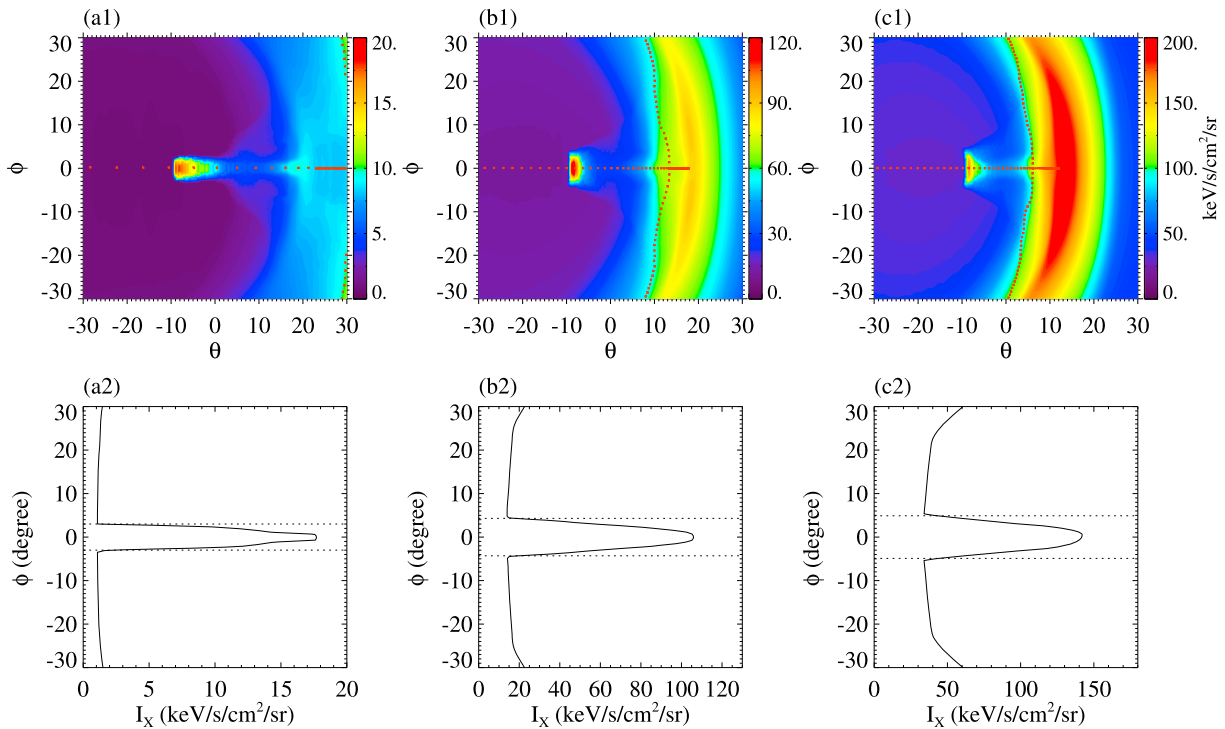


Figure 9. X-ray images of the cusp region and magnetosheath for Cases 1 (a1), 2 (b1), and 3 (c1). The hypothetical satellite is at $(10.42, -0.0062, 5.43) R_E$, that is, point B in Figure 4, and the X-ray telescope points to $(6.33, 0, 0) R_E$. The red lines mark the magnetopause positions in the equatorial and noon-midnight meridian planes by mapping the magnetohydrodynamic results to the image coordinate. Figures 9a2 to 9c2 show the relationship between I_X and ϕ at $\theta = -8.4^\circ$ for the three simulation runs.

background. The occurrence of a sudden increase in the X-ray intensity gradient can be considered the boundary of the cusp. More specifically, we found that the following criterion works well for the simulation runs:

$$dI_X/d\phi \geq 20\%(I_{X_{\max}} - I_{X_{\min}}) \text{ per degree,} \quad (3)$$

where $I_{X_{\max}}$ and $I_{X_{\min}}$ are the maximum and minimum X-ray intensity along the direction perpendicular to the cusp boundary (i.e., roughly the direction with fixed θ here). The lower panel of Figure 9 shows the variation of X-ray intensity along the ϕ direction, with $\theta = -8.4^\circ$. The dashed lines indicate the boundary of the cusp region at $\phi = \pm\phi_0$, which is related to the dimension of cusp along the azimuthal direction for the specific geometry. The line of sight is almost perpendicular to the azimuthal direction, and hence the local time extension L can be estimated by $L_{X\text{-ray}} \sim 2r_0 \sin \phi_0$, where r_0 is the distance from the satellite to the cusp boundary. Although it is not possible to derive the exact position of the cusp boundary from the X-ray image since r_0 is unknown, the variations of the scale under different solar wind conditions can be deduced. Table 3 shows the estimation of this variation by analyzing the MHD simulation results and the X-ray images. The azimuthal scale of cusp from MHD simulation can be estimated by $L_{\text{MHD}} \sim 2r \sin A$, where the angle A is half of the local time extension of the cusp region from MHD results, and r is the geocentric distance for the cusp boundary. The magnetic field for the low-altitude cusp is basically the dipole field, and thus the cusp boundary in the azimuthal direction varies along the dipole field lines at different

Table 3
Azimuthal Scale (L) of Cusp Under Different Solar Wind Conditions

Run	L_{MHD}	$L_{\text{MHDi}}/L_{\text{MHDj}}$	$L_{X\text{-ray}}$	$L_{X\text{-rayi}}/L_{X\text{-rayj}}$
Case 1	$2r \sin 20^\circ$	—	$2r_0 \sin 3.0^\circ$	—
Case 2	$2r \sin 32^\circ$	1.55 (case2/case1)	$2r_0 \sin 4.3^\circ$	1.43 (case2/case1)
Case 3	$2r \sin 34^\circ$	1.64 (case3/case1)	$2r_0 \sin 4.9^\circ$	1.63 (case3/case1)

Note. i and j are the labels for different MHD simulation cases. MHD = magnetohydrodynamic.

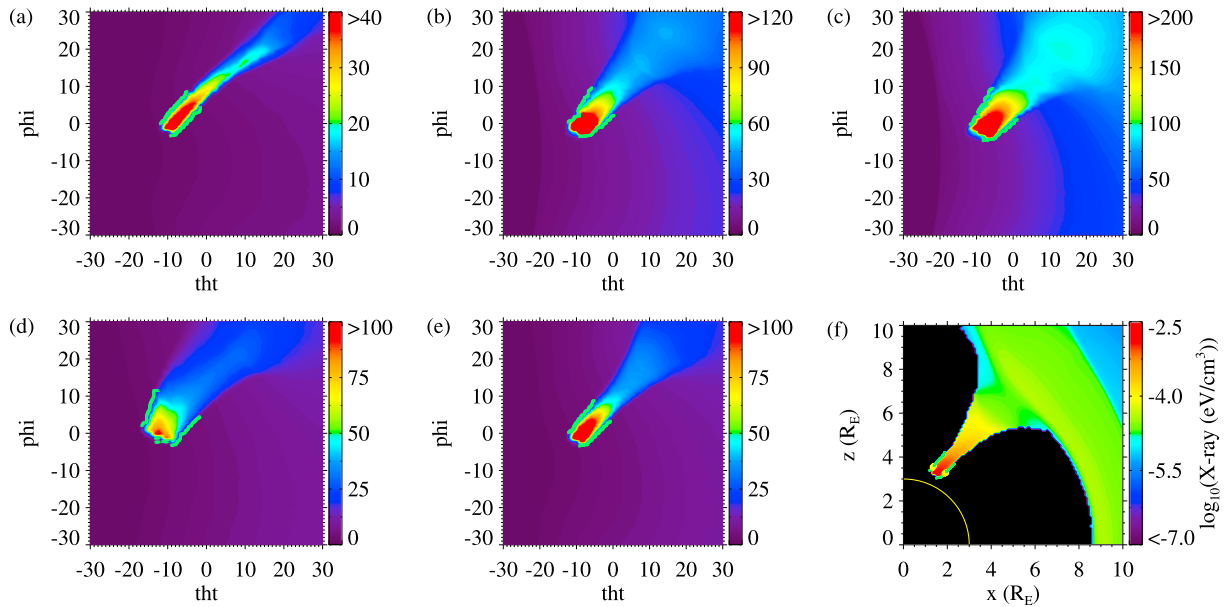


Figure 10. X-ray images of the northern cusp detected by a hypothetical satellite at $(2.41, -5.63, 3.37) R_E$ pointing to the noon-midnight meridian plane, for Cases 1 to 5 (a–e). The green lines are the cusp boundaries identified from the X-ray images. Panel (f) shows the cusp region in the meridian plane for Case 5, by plotting the contours of X-ray emissivity. The green lines are plotted by mapping the cusp boundary in (e) to the noon-midnight meridian plane, and the two orange dots are the equatorward and poleward boundaries at $r = 3.8R_E$, which are used to calculate the latitude of cusp boundary on the ground.

altitudes. This means that the angle A is almost the same at different values of r for low-altitude cusp. We list the values for $r = 3.7R_E$ here in the second column, and changing to other altitudes does not apparently alter the results. In the fourth column, the angle φ_0 is the averaged value for θ angle ranging from -8.0° to -8.4° , at the low-altitude cusp region. It is seen from Table 3 that enhancement of solar wind flux will lead to increase in the cusp scale on the azimuthal direction, and the extent of the increases can be derived by analyzing the X-ray images. The azimuthal scales of cusp do not exhibit any significant difference under different IMF B_z orientations in our simulation, so they are not shown here.

To study the latitude of the cusp boundaries, we pick an appropriate point on an orbit with 67° inclination (an alternative option for SMILE): $(2.41, -5.63, 3.37) R_E$, that is, point C in Figure 4b2. If the telescope points to $(2.41, 0, 3.37) R_E$, the X-ray images for all the studied cases are simulated and presented in Figure 10. It is noticed that for this viewing geometry, the Earth would be at $\theta = -23.2^\circ$ and $\varphi = -30.9^\circ$, outside of the FOV of SMILE, so that the cusp image will not be contaminated by the large X-ray emissions from the Earth. The increase of the northern cusp scale along the latitudinal direction is visible from Figures 10a to 10c. The equatorward motion of cusp after IMF southward turning is also evident in the figure. More quantitative study can be performed under this specific viewing geometry with the instrument pointing perpendicular to the noon-midnight meridian plane. The cusp boundaries are identified from the X-ray images by using equation (2), marked by the green lines in Figures 10a–10e. These boundaries in the image coordinate are then converted to the GSM coordinate to show the cusp boundary in the noon-midnight meridian plane.

Table 4

Latitude of the Cusp Boundary on the Ground Under Different Solar Wind Conditions

Run	Lat_{equMHD}	Lat_{polMHD}	$Lat_{\text{equX-ray}}$	$Lat_{\text{polX-ray}}$
Case 1	75.9	79.5	75.5	79.4
Case 2	74.7	79.3	74.4	79.5
Case 3	73.7	78.8	73.4	79.2
Case 4	76.1	83.2	75.8	83.7
Case 5	75.5	79.5	75.0	79.6

Note. MHD = magnetohydrodynamic.

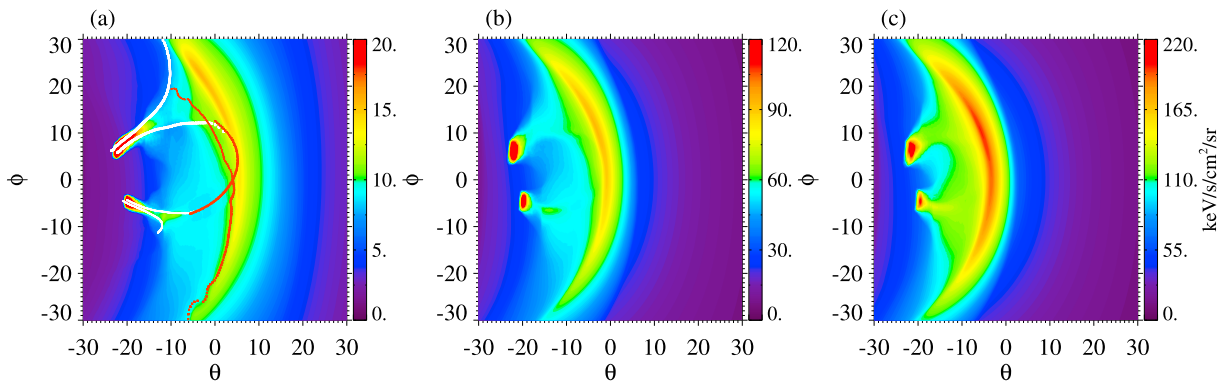


Figure 11. X-ray images for Cases 1 (a), 2 (b), and 3 (c) with a more general viewing geometry. The hypothetical satellite is at $(4.17, -9.70, 16.64) R_E$, that is, point D in Figure 4b2, and the X-ray telescope points to $(8.72, 0, 0) R_E$. The white lines in (a) mark the boundary positions for northern (thick lines) and southern (thin lines) cusps, depicted in Figure 4a2. The red lines show the mapping of the equatorial and noon-midnight meridian magnetopause in Figures 4a1 and 4a2 to the image coordinate.

The green lines in Figure 10f are the equatorward and poleward boundaries of the cusp region analyzed from the X-ray images for Case 5. It is seen that the boundaries match well with the MHD result (the background are contours of the X-ray emissivity in the meridian plane).

The low-altitude boundary positions are then mapped along the dipole field lines to calculate the latitudes of cusp region on the ground. Table 4 lists the latitude of cusp derived from MHD and X-ray images under different solar wind conditions. It is seen by comparing Cases 1–3 that the equatorward boundary of cusp apparently moves toward a lower latitude with increasing solar wind flux, causing the increase of the cusp scale along the latitudinal direction. Cases 4 and 5 show that the cusp region shifts to a lower latitude during southward IMF, related to the reconnection on the dayside magnetopause. The differences of the cusp boundaries identified from X-ray images and those obtained directly from the MHD results are smaller than 0.5° for all the studied cases.

3.4. X-ray Images With a More General Viewing Geometry

The responses of the magnetopause and cusps to variations in the solar wind are analyzed from X-ray images with specific viewing geometries in the above sections. These viewing geometries are special so that we can use certain assumptions to derive the magnetopause or cusp positions, while at the same time, they are appropriate to the SMILE orbit, satellite positions and pointing directions. For a more general viewing geometry, such as point D in Figure 4b2 from $(4.17, -9.70, 16.64) R_E$ to $(8.72, 0, 0) R_E$, the X-ray images are shown in Figure 11. This point D is close to the apogee on the orbit with $\sim 67^\circ$ inclination. It is discernible in the figure that the dimension of the magnetopause is smaller and the spreading of cusp is larger with increased solar wind flux. However, quantitative analysis of the responses are not straightforward, as the viewing geometry prevents us from making simple assumptions to directly invert the exact positions of the magnetopause and/or cusp from the X-ray images. The advanced methods proposed by Jorgensen et al. (2017) and Collier and Connor (2018), which reconstruct the magnetopause by finding the best match between parametric models and the observed X-ray image and by studying a series of tangent observations, respectively, will help with the quantitative analysis, although this analysis is beyond the main scope of this research.

4. Discussion and Conclusion

Based on the PPMLR-MHD simulations, we present the soft X-ray emissions from SWCX in the Earth's magnetosheath and cusps under different solar wind conditions. Cases 1–3 have different solar wind flux, and Cases 4 and 5 compare the effect of different IMF B_z orientations. The X-ray images are simulated for each case, and these images could capture the main responses of the magnetopause and cusp regions. Good agreement in the cusp and magnetopause positions was found between the MHD model and the X-ray images. With certain viewing geometries, the magnetopause position in the equatorial plane, as well as the latitudinal scales and azimuthal extent of cusp can be derived directly from the 2-D X-ray images. These reconstructed positions help the quantitative study of magnetospheric responses to solar wind

changes on a global scale. Basic issues in the space physics domain such as the magnetic reconnection and energy/momentum transportation are expected to be explored with the help of an X-ray telescope. Therefore, our current simulation confirms that the X-ray imaging is an elegant approach to study the magnetospheric responses to solar wind variations. It is also noted that the present study is performed under quasi-steady conditions. Images taken under constant solar wind conditions could be viewed as default images (like a library reference) and images taken during periods with rapid changes of the solar wind could be measured against this default to monitor the temporal effects. In future studies, more detailed discussion about the temporal effects on X-ray images will be analyzed by using real solar wind as the input. For instance, a geomagnetic storm event similar to the one presented by Branduardi-Raymont et al. (2016) is under calculation with high spatial resolution. Finally, we also note that this paper does not focus on proposing a general inversion algorithm. We only use several typical viewing geometries to study whether we can extract the desired information from simply analyzing the X-ray images. The development of reconstruction techniques is an important issue for future studies, and several groups are currently working on this (e.g., Collier & Connor, 2018; Jorgensen et al., 2017).

Acknowledgments

The authors thank Y. Q. Hu for providing information on the MHD simulation code, from which the data used in this study are derived. The data for X-ray images studied in this paper can be downloaded from Zenodo (<https://doi.org/10.5281/zenodo.1415285>). This work was supported by NNSFC grants 41774173, 41731070, and 41574159, Key Research Program of Frontier Sciences, CAS, grant QYZDJ-SSW-JSC028, Strategic Pioneer Program on Space Science, CAS, grants XDA15052500, XDA15350201, and in part by Research Fund from the Chinese Academy of Sciences and the Specialized Research Fund for State Key Laboratories of China. The author Tianran Sun is also supported by the Young Elite Scientists Sponsorship Program by CAST (2017QNR001) and the Youth Innovation Promotion Association (2016134).

References

- Bhardwaj, A., Elsner, R. F., Randall Gladstone, G., Cravens, T. E., Lisse, C. M., Dennerl, K., et al. (2007). X-rays from solar system objects. *Planetary and Space Science*, *55*, 1135–1189.
- Branduardi-Raymont, G., Escoubet, C. P., Kuntz, K., Lui, T., Read, A., Sibeck, D., et al. (2016). Link between solar wind, magnetosphere, and ionosphere, ISSI-BJ magazine, No. 9.
- Branduardi-Raymont, G., Sembay, S. F., Eastwood, J. P., Sibeck, D. G., Abbey, T. A., Brown, P., et al. (2012). AXIOM: Advanced X-ray imaging of the magnetosphere. *Experimental Astronomy*, *33*, 403–443. <https://doi.org/10.1007/s10686-011-9239-0>
- Branduardi-Raymont, G., Wang, C., & SMILE Team (2016). SMILE (Solar Wind Magnetosphere Ionosphere Link Explorer) : X-ray imaging of the Sun-Earth connection. In *XMM-Newton: The Next Decade(2016)*, pp. 81.
- Carter, J. A., & Sembay, S. (2008). Identifying XMM-Newton observations affected by solar wind charge exchange—Part I. *Astronomy & Astrophysics*, *489*, 837–848.
- Carter, J. A., Sembay, S., & Read, A. M. (2010). A high charge state coronal mass ejection seen through solar wind charge exchange emission as detected by XMM-Newton. *Monthly Notices of the Royal Astronomical Society*, *402*, 867–878.
- Carter, J. A., Sembay, S., & Read, A. M. (2011). Identifying XMM-Newton observations affected by solar wind charge exchange—Part II. *Astronomy & Astrophysics*, *527*, A115.
- Chapman, S., & Bartels, J. (1940). *Geomagnetism*. Oxford: Oxford University Press.
- Collier, M. R., & Connor, H. K. (2018). Magnetopause surface reconstruction from tangent vector observations. *Journal of Geophysical Research: Space Physics*, *123*, 10,189–10,199. <https://doi.org/10.1029/2018JA025763>
- Collier, M. R., Porter, F. S., Sibeck, D. G., Carter, J. A., Chiao, M. P., Chornay, D., et al. (2012). Prototyping a global soft X-ray imaging instrument for heliophysics, planetary science, and astrophysics science. *Astronomische Nachrichten*, *333*(4), 378–382.
- Collier, M. R., Sibeck, D. G., Cravens, T. E., Robertson, I. P., & Omid, N. (2010). Astrophysics noise: A space weather signal. *Eos, Transactions American Geophysical Union*, *91*(24), 709–722.
- Collier, M. R., Snowden, S. L., Sarantos, M., Benna, M., Carter, J. A., Cravens, T. E., et al. (2014). On lunar exospheric column densities and solar wind access beyond the terminator from ROSAT soft X-ray observations of solar wind charge exchange. *Journal of Geophysical Research: Planets*, *119*, 1459–1478. <https://doi.org/10.1002/2014JE004628>
- Connor, H. K., & Carter, J. (2017). Exospheric Neutral density at the Earth's subsolar magnetopause deduced from the XMM-Newton X-ray observations. In *AGU fall meeting 2017*, Abstract SM31D-05.
- Cravens, T. E. (1997). Comet Hyakutake X-ray source: charge transfer of solar wind heavy ions. *Geophysical Research Letters*, *24*(1), 105–108.
- Cravens, T. E. (2000). Heliospheric X-ray emission associated with charge transfer of the solar wind with interstellar neutrals. *The Astrophysical Journal*, *532*, L153–L156.
- Cravens, T. E., Robertson, I. P., & Snowden, S. L. (2001). Temporal variations of geocoronal and heliospheric X-ray emission associated with the solar wind interaction with neutrals. *Journal of Geophysical Research*, *106*(A11), 24,883–24,892.
- Dennerl, K. (2002). Discovery of X-rays from Mars with Chandra. *Astronomy & Astrophysics*, *394*, 1119–1128.
- Escoubet, C. P., Bosqued, J. M., Berchem, J., Trattner, K. J., Taylor, M. G. G. T., Pitout, F., et al. (2006). Temporal evolution of a staircase ion signature observed by Cluster in the mid-altitude polar cusp. *Geophysical Research Letters*, *33*, L07108. <https://doi.org/10.1029/2005GL025598>
- Florinski, V., Guo, X., Balsara, D. S., & Meyer, C. (2013). Magnetohydrodynamic modeling of solar system processes on geodesic grids. *The Astrophysical Journal Supplement*, *205*(19), 12. <https://doi.org/10.1088/0067-0049/205/2/19>
- Fujimoto, R., Mitsuda, K., McCammon, D., Takei, Y., Bauer, M., Ishisaki, Y., et al. (2007). Evidence for solar-wind charge-exchange X-ray emission from the Earth's magnetosheath. *Publications of the Astronomical Society of Japan*, *59*, 133–140.
- Hodges, R. R. (1994). Monte Carlo simulation of the terrestrial hydrogen exosphere. *Journal of Geophysical Research*, *99*(A12), 23,229–23,247.
- Hu, Y. Q., Guo, X. C., & Wang, C. (2007). On the ionospheric and reconnection potentials of the Earth: Results from global MHD simulations. *Journal of Geophysical Research*, *112*, A07215. <https://doi.org/10.1029/2006JA012145>
- Jorgensen, A. M., Sun, T., Wang, C., Dai, L., Sembay, S., Wei, F., & Ronglan, X. (2017). Boundary detection in three dimensions with application to the SMILE mission. In *2017 AGU Fall Meeting*. Abstract SM13A-2195.
- Kuntz, K. D., Collado-Vega, Y. M., Collier, M. R., Connor, H. K., Cravens, T. E., Koutroumpa, D., et al. (2015). The solar wind charge-exchange production factor for hydrogen. *Astronomy & Astrophysics*, *808*, 143. <https://doi.org/10.1088/0004-637X/808/2/143>
- Lisse, C. M., Dennerl, K., Englhauser, J., Harden, M., Marshall, F. E., Mumma, M. J., et al. (1996). Discovery of X-ray and extreme ultraviolet emission from Comet C/Hyakutake. *Science*, *274*(5285), 205–209.

- Ness, N. F., Scarce, C. S., & Cantarano, S. (1966). Preliminary results from the Pioneer-6 magnetic field experiment. *Journal of Geophysical Research*, *71*, 3305–3313.
- Newell, P. T., & Meng, C.-I. (1994). Ionospheric projections of magnetospheric regions under low and high solar wind pressure conditions. *Journal of Geophysical Research*, *99*, 273–286.
- Newell, P. T., Meng, C.-I., & Sibeck, D. G. (1989). Some low-altitude cusp dependencies on the interplanetary magnetic field. *Journal of Geophysical Research*, *94*, 8921–8927.
- Pepino, R., Kharchenko, V., Dalgarno, A., & Lallement, R. (2004). Spectra of the X-ray emission induced in the interaction between the solar wind and heliospheric gas. *The Astrophysical Journal*, *617*, 1347–1352.
- Pitout, F., Escoubet, C. P., Klecker, B., & Reme, H. (2006). Cluster survey of the mid-altitude cusp: 1. Size, location, and dynamics. *Annals of Geophysics*, *24*(11), 3011–3026.
- Robertson, I. P., Collier, M. R., Cravens, T. E., & Fok, M.-C. (2006). X-ray emission from the terrestrial magnetosheath including the cusps. *Journal of Geophysical Research*, *111*, A12105. <https://doi.org/10.1029/2006JA011672>
- Robertson, I. P., & Cravens, T. E. (2003). X-ray emission from the terrestrial magnetosheath. *Geophysical Research Letters*, *30*(8), 1439. <https://doi.org/10.1029/2002GL016740>
- Sibeck, D. G., Allen, R., Aryan, H., Bodewits, D., Brandt, P., Branduardi-Raymont, G., et al. (2018). Imaging plasma density structures in the soft X-rays generated by solar wind charge exchange with neutrals. *Space Science Reviews*, *214*, 124. <https://doi.org/10.1007/s11214-018-0504-7>
- Snowden, S. L., Collier, M. R., Cravens, T., Kuntz, K. D., Lepri, S. T., Robertson, I., & Tomas, L. (2009). Observation of solar wind charge exchange emission from exospheric material in and outside Earth's magnetosheath 2008 September 25. *The Astrophysical Journal*, *691*, 372–381.
- Sun, T. R., Wang, C., Wei, F., & Sembay, S. (2015). X-ray imaging of Kelvin-Helmholtz waves at the magnetopause. *Journal of Geophysical Research: Space Physics*, *120*, 266–275. <https://doi.org/10.1002/2014JA020497>
- Walsh, B. M., Collier, M. R., Kuntz, K. D., Porter, F. S., Sibeck, D. G., Snowden, S. L., et al. (2016). Wide field-of-view soft X-ray imaging for solar wind-magnetosphere interactions. *Journal of Geophysical Research: Space Physics*, *121*, 3353–3361. <https://doi.org/10.1002/2016JA022348>
- Wang, C., Li, Z. J., Sun, T. R., Liu, Z. Q., Liu, J., Wu, Q., et al. (2017). SMILE satellite mission survey. *Space International (in Chinese)*, *464*, 13–16.
- Wargelin, B. J., Kornbleuth, M., Martin, P. L., & Juda, M. (2014). Observation and modeling of geocoronal charge exchange X-ray emission during solar wind gusts. *The Astrophysical Journal*, *796*, 14. <https://doi.org/10.1088/0004-637X/796/1/28>
- Whittaker, I. C., & Sembay, S. (2016). A comparison of empirical and experimental O7+, O8+, and O/H values, with applications to terrestrial solar wind charge exchange. *Geophysical Research Letters*, *43*, 7328–7337. <https://doi.org/10.1002/2016GL069914>
- Whittaker, I. C., Sembay, S., Carter, J. A., Read, A. M., Milan, S. E., & Palmroth, M. (2016). Modeling the magnetospheric X-ray emission from solar wind charge exchange with verification from XMM-Newton observations. *Journal of Geophysical Research: Space Physics*, *121*, 4158–4179. <https://doi.org/10.1002/2015JA022292>
- Zhang, B., Brambles, O., Lotko, W., Dunlap-Shohl, W., Smith, R., Wiltberger, M., & Lyon, J. (2013). Predicting the location of polar cusp in the Lyon-Fedder-Mobarry global magnetosphere simulation. *Journal of Geophysical Research: Space Physics*, *118*, 6327–6337. <https://doi.org/10.1002/jgra.50565.1>